Cone cell dysfunction attenuates retinal neovascularization in oxygen-induced retinopathy mouse model

Running title: Cone cell dysfunction attenuates neovascularization

Jun Wu[1, 2], Dong Hyun Jo[3], Marcus Fruttiger[4, *] and Jeong Hun Kim[1, 2, 5, 6, 7 **]

[1]Fight against Angiogenesis-Related Blindness (FARB) Laboratory, Biomedical research institute, Seoul National University Hospital, Seoul 03082, Republic of Korea

[2]Department of Biomedical Sciences, Seoul National University College of Medicine, Seoul 03080, Republic of Korea

[3]Department of Anatomy and Cell Biology, Seoul National University College of Medicine, Seoul 03080, Republic of Korea

[4]UCL Institute of Ophthalmology, University College London, London WC1E 6BT, United Kingdom

[5]Department of Ophthalmology, Seoul National University College of Medicine, Seoul 03080, Republic of Korea

[6]Global Excellence Center for Gene & Cell Therapy (GEC-GCT), Seoul National University Hospital, Seoul 03080, Republic of Korea

[7]Institute of Reproductive Medicine and Population, Seoul National University College of Medicine, Seoul 03080, Republic of Korea

[*]***Correspondence author*:**

Marcus Fruttiger, UCL Institute of Ophthalmology, University College London, London WC1E 6BT, United Kingdom.

E-mail address: m.fruttiger@ucl.ac.uk

***Correspondence author:*

Jeong Hun Kim, Department of Biomedical Sciences & Ophthalmology, Seoul National University College of Medicine, Seoul 03080, Republic of Korea.

E-mail address: steph25@snu.ac.kr

Key words: Cone cell dysfunction, Neovascularization, Oxygen-induced retinopathy

Abstract

Aberrant neovascularization is the most common feature of in retinopathy of prematurity (ROP), which leads to retinal detachment and visual defects in neonates with a low gestational age eventually. Understanding the regulation of inappropriate angiogenic signaling benefits individuals at-risk. Recently, neural activity originating from the specific neural activity has been considered to contribute to retinal angiogenesis. Here, we explored the impact of cone cell dysfunction on oxygen-induced retinopathy (OIR), a mouse model commonly employed to understand retinal diseases associated with abnormal blood vessel growth, using the *Gnat2*^{cpfl3} (cone photoreceptor function loss-3) strain of mice (regardless the sex), which is known for its inherent cone cell dysfunction. We found that the retinal avascular area, hypoxic area and neovascular area were significantly attenuated in *Gnat2*^{cpfl3} OIR mice compared to those in C57BL/6 OIR mice. Moreover, the HIF-1α/VEGF axis was also reduced in *Gnat2*^{cpfl3} OIR mice. Collectively, our results indicated that cone cell dysfunction, as observed in *Gnat2*^{cpfl3} OIR mice, leads to attenuated retinal neovascularization. This finding suggests that retinal neural activity may precede and potentially influence the onset of pathological neovascularization.

Significance

Retinal neovascularization rarely occurs in patients or animal models with retinal degeneration. This is thought to be associated with the significantly reduced number of retinal cells. However, recent experimental data have shown that inhibiting neural activity driven by specifical retinal cells can disrupt retinal deep-layer angiogenesis and reduce pathological neovascularization in oxygen-induced retinopathy (OIR) mouse models, even in the absence of changes in cell number. Herein, using an OIR mouse model revealed that cone cell dysfunction attenuated retinal neovascularization. These findings further provide insight into the retinal neural activity that may precede and potentially influence the onset of pathological neovascularization.

1 INTRODUCTION

Retinopathy of prematurity (ROP), formerly known as retrolental fibroplasia, contributes to blindness in neonates of a low gestational age (Hellström, Smith, & Dammann, 2013). This condition primarily arises from incomplete vascularization, which leads to retinal hypoxia and subsequent neovascularization. Characteristically, ROP induces neovascularization that penetrates the inner limiting membrane towards the vitreous (Sapieha et al., 2010). These pathological neovessels, being leaky and fibrotic, can cause retinal detachment and, blindness eventually. Hence, it is essential to delve deeper into the disease mechanisms and understand how to inhibit pathological angiogenesis, thereby benefiting individuals at-risk.

Researchers have relied on the oxygen-induced retinopathy (OIR) mouse model to investigate these pathological mechanisms. This model is particularly valuable because it shares many characteristics with human retinal ischemic diseases and allows for easy genetic manipulation (Connor et al., 2009; Kim, D'Amore, & Connor, 2016; Liu, Wang, Sun, & Chen, 2017; Smith et al., 1994; Vähätupa, Järvinen, & Uusitalo-Järvinen, 2020). Previous studies have demonstrated restrained retinal neovascularization in early onset retinal degeneration mouse models (Zhang & Zhang, 2014). Another study observed a near absence of neovascularization in *Pde6b*^{rd1} OIR mice, which rapidly lost photoreceptors during the suckling age (Scott, Powner, & Fruttiger, 2014). These findings suggested an inverse relationship between angiogenesis and retinal degeneration, leading to the hypothesis that photoreceptor loss results in lower oxygen consumption, creating a relatively 'hyperoxic state' that inhibits angiogenesis in the retinal microenvironment (Pennesi, Nishikawa, Matthes, Yasumura, & LaVail, 2008; Zhang & Zhang, 2014). Conversely, Weiner et al. found that the inhibition of cholinergic neural activity driven by starburst amacrine cells can disrupt retinal deep-layer angiogenesis and reduce pathological neovascularization in OIR mouse models, suggesting the

53 importance of neurovascular crosstalk in retinal angiogenesis (Weiner et al., 2019). These
54 diverse results raise intriguing questions regarding the potential role of photoreceptor activity
55 in pathological neovascularization.

56 The cone photoreceptor function loss-3 (cpfl3) mouse model, an established model of
57 achromatopsia-4, carries a missense mutation in the α-subunit of cone transducin (Gnat2),
58 leading to abnormal cone cell activity (Chang et al., 2006). Leveraging these insights, we aimed
59 to investigate the role of cone cell dysfunction in the OIR mouse model.

2 METHODS AND MATERIALS

2.1 Animals and OIR model establishment

All animals used in this study and breeding adhered to the statement of the Association for Research in Vision and Ophthalmology (ARVO) and reported in compliance with Animal Research: Reporting of In Vivo Experiments (ARRIVE) guidelines. The animal protocols were reviewed and approved by the Seoul National University Animal Care and Use Committee. The C57BL/6 (cat. no. 000664) and *Gnat2*^{cpfl3} (cat. no. 006795) mice were purchased from the Jackson Laboratory (Bar Harbor, Maine, USA). The C57BL/6 (IACUC no. SNU-180327) and *Gnat2*^{cpfl3} (IACUC no. SNU-210104) mice were bred at the Biomedical Center for Animal Resource Development of the Seoul National University. Mice were bred by cross two homozygous individuals. Mice were kept in approved cages under cyclic light conditions (12-h on/12-h off) with ad libitum access to food and water. The OIR model was induced in C57BL/6 and *Gnat2*^{cpfl3} mice. Briefly, newborn pups (regardless the sex) and their nursing dam were placed in 75 ± 0.5% oxygen in an O_2-regulated chamber with an oxygen controller (Pro-Ox 110 Chamber Controller; Biospherix, Redfield, NY, USA) from P7 to P12. At P12, the mice were placed back into room air (21% oxygen). Those mice with weight less than 5 g and more than 7.5 g were excluded at P17 (Stahl et al., 2010). Five dams (12-16 weeks of age, five independent litters) and 40 pups of each group were used in this study.

2.2 Retinal whole-mount preparation and Immunofluorescence staining

Retinal whole-mount preparations were performed as previously described by our group (Park, Kim, Park, & Kim, 2015). Pups from each strain were randomly selected and euthanized by carbon dioxide (CO_2) inhalation. The ocular globe was enucleated and fixed in 4% paraformaldehyde (PFA, P2031; Biosesang, Yongin, KR) for 30 min at room temperature. The

cornea and lens were removed, then the retina was dissociated from the retinal pigment epithelial/choroid/sclera complex. The retina was incubated in blocking solution (BP150; Biosolution, Yongin, KR) at room temperature for 2 hours and stained with Alexa Fluor 488-conjugated anti-IB4 antibody (1:250, I21411; Invitrogen, Carlsbad, CA, USA, RRID:AB_2314662) overnight at 4℃. Subsequently, the stained retina was placed on a glass slide with the photoreceptor cells layer against it. An adequate amount of mounting solution was added, and a cover slide was placed. The avascular area and neovascular tufts area were quantitatively analyzed using ImageJ 1.42 software (National Institutes of Health, Bethesda, MD, USA, RRID:SCR_003070). Data analyses were conducted by one operator blinded to group allocation.

2.3 Assessment of tissue hypoxia

To detect the retinal hypoxia, the mice received the Hypoxyprobe™ Red549 Kit (HP, 60 mg/kg, HP7-100; Hypoxyprobe, Inc, Burlington, MA, USA) via intraperitoneal injection at P14. After 30 min, the mice were euthanized by CO_2 inhalation. The globes were harvested and fixed in 4% PFA for 30 min at room temperature. The retina was then dissociated and incubated in mouse IgG1 monoclonal antibody conjugated to Dylight™549 fluorophore (1:50, red-549-mab; Hypoxyprobe, Inc, Burlington, MA, USA) overnight at 4°C. The following day, the retinas were rinsed three times and stained with Alexa Fluor 488-conjugated anti-IB4 antibody for 2 hours at room temperature. The retinal hypoxic area in the whole-mounted retina was divided by the total measured retinal area and presented as a percentage using ImageJ software. The fluorescence intensity was analyzed in retinal cross-section images. The samples were stained with the Dylight™549 fluorophore overnight at 4°C. After washing with phosphate-buffered saline (PBS), the samples were counterstained with 10 mg/mL of DAPI (1:1000; D9542;

Sigma-Aldrich, St. Louis, MO, USA) at room temperature for 15 min. The fluorescence intensity was assessed using ImageJ software. All analyzers were blind to the genotype of the mice.

2.4 Protein extraction and western blot analysis

The retinas were harvested at P14, and protein was extracted using a radioimmunoprecipitation (RIPA) buffer (RC2002-050; Biosesang, Yongin, KR) containing protease inhibitor (p3100-001; GenDEPOT, Katy, TX, USA) and phosphatase inhibitor (p3200-001; GenDEPOT, Katy, TX, USA). The concentration of each sample was determined using the BCA Protein Quantitation Kit (23228; ThermoFisher, Waltham, MA, USA), and then the retinal lysates (30-50 μg) were loaded in the gels and samples were separated with SDS-PAGE and transferred to polyvinylidene difluoride filter membranes. The membranes were blocked with 5% skim milk in TBST (TBS containing 0.1% Tween) at room temperature for 1 hour and then incubated with primary antibodies overnight at 4°C. The following primary antibodies were used: mouse anti-β-actin monoclonal antibody (1:10000, A1978; Sigma-Aldrich Corp., St. Louis, MO, USA, RRID:AB_476692), mouse anti-VEGF (vascular endothelial growth factor) monoclonal antibody (1:1000, SC-7269; Santa Cruz Biotechnology, Dallas, TX, USA, RRID:AB_628430), mouse anti-HIF-1α (hypoxia-inducible factor 1 alpha) monoclonal antibody (1:1000, sc-13515; Santa Cruz Biotechnology, Dallas, TX, USA, RRID:AB_627723), rabbit anti-p-PDE6γ (phosphodiesterase 6) polyclonal antibody (1:1000, PA5-106023; Invitrogen, Carlsbad, CA, USA, RRID:AB_2817422). The following day, the membranes were incubated with the secondary antibodies for 1 hour at room temperature. The horse anti-mouse IgG antibody (1:5000, 7076; Cell Signaling Technology, Danvers, MA, USA, RRID:AB_330924) and goat anti-rabbit IgG (1:5000, 7074; Cell Signaling Technology, Danvers, MA, USA,

RRID:AB_2099233) were used. The blots were treated with enhanced chemiluminescence reagent (34095; ThermoFisher, Waltham, MA, USA) to detect the protein bands. The resulting blot images were recorded using the Amersham™ Imager 680 (GE Healthcare Bio-Sciences AB, Sweden) and the bands were quantified using ImageJ software.

2.5 Histology

The mice were euthanized, and the globes were fixed in Hartman's fixative solution (H0290; Sigma-Aldrich Corp., St. Louis, MO, USA) and 4% PFA for 20 hours at room temperature, respectively. After fixation, 'windows' were made on the eyeball at the location of the anterior and posterior chambers, as described previously (Pang et al., 2021). Briefly, the eye was held in place with forceps, and created a slight incision with a 26-gauge needle was made into the anterior chamber. This step was repeated in the posterior part of the eyeball, which was aligned with the window in the anterior chamber. The globes were embedded in paraffin. After 4-μm-thick paraffin sections were prepared, the sections were deparaffinized and hydrated by sequential immersion in graded ethyl alcohol solutions and xylene substitute (6764506; Epredia, Kalamazoo, MI, USA). Hematoxylin and eosin (H&E) staining was performed for histological examination. The retinal thickness from the inner limiting membrane to the retinal pigment epithelial layer was measured using NIS-Elements Imaging Software (Nikon Instruments Inc., Melville, NY, USA, RRID:SCR_014329), at the position approximately 200 μm from the optic disc. The mean number of cells in the retinal outer nuclear layer (ONL) were counted per 20 μm in a 400× magnification section by at least two observers. The number of neovascular endothelial cell nuclei on the vitreous side of the inner limiting membrane was counted at 400× magnification images.

2.6 Electroretinography

Mice were anesthetized with an intraperitoneal injection of tiletamine (25 mg/mL)/zolazepam (25 mg/mL) mixture. Pupils were dilated with an eye drop containing phenylephrine hydrochloride (5 mg/mL) and tropicamide (5 mg/mL). The recording electrode was placed on the corneal surface, and the reference needle electrode was placed subcutaneously on the head, while the electrode in the tail served as the ground. Full-field electroretinography (ERG) was performed using the Electrophysiologic System 3000 (UTAS E-3000, LKC Technologies Inc., Gaithersburg, MD, USA). Prior to scotopic ERG, mice were kept in the dark overnight. In the dark-adapted condition, the scotopic responses were recorded using a single dim flash of 0 dB using a notch filter at 60 Hz and a digital bandpass filter ranging from 0.3 to 500 Hz. After recording scotopic responses, the mice were exposed to light for at least 15 min. In the light-adapted condition, the photopic responses were recorded in response to a single flash of 0 dB using a notch filter at 60 Hz and a digital bandpass filter ranging from 0.3 to 500 Hz. The amplitude of the a-wave was measured from the baseline to the lowest negative going voltage, whereas the peak b-wave amplitudes were measured from the trough of the a-wave to the highest peak of the positive b-wave. The ERG waveforms were analyzed using GraphPad Prism 9 (GraphPad Software, San Diego, CA, USA, RRID:SCR_002798).

2.7 Optical coherence tomography

The optical coherence tomography (OCT) device was manufactured by the Korean Research Institute of Standards and Science (KRISS). After anesthetization, the fully dilated pupil was directed towards the subjective lens. Eyes were kept moisturized with PBS solution during the entire procedure to ensure optimized images. The thickness of the retinal layers was manually measured on the OCT projection image. The measurement axis was perpendicular from the

inner limiting membrane to the retinal pigment epithelial layer, at the position approximately 200 μm from the optic head.

2.8 Statistical analysis

Statistical significance was calculated using GraphPad Prism 9. To compare between two groups, an unpaired t-test or Mann–Whitney test was employed. Initially, all data were assessed for normal distribution. If the data followed a normal distribution, an unpaired t-test was used to identify significant differences. In the case of non-normal distribution, a Mann–Whitney test was applied. Considering the normal distribution and homogeneity of variance data, two-way ANOVA with Bonferroni's post hoc tests was used for multiple comparisons. Boxplots were used to present all quantitative data. Dot plots are used to indicate individual samples. Differences were considered significant at the level of $p < .05$.

3 RESULTS

3.1 Slow retinal degeneration in *Gnat2*^{cpfl3} mice

We performed H&E staining of paraffin-sections from C57BL/6 and *Gnat2*^{cpfl3} room air (RA, not undergone hyperoxia) mice at P17 and 6 months to characterize the retinal histopathological and morphometric changes in this strain (Figure 1a, d). Retinal thickness, assessed by measuring the distance between the inner limiting membrane to the retinal pigment epithelial layer, was not significantly different between C57BL/6 and *Gnat2*^{cpfl3} RA mice at P17 and 6 months (Figure 1b, $n = 5$, unpaired t-test, $t_{(8)} = .1243$, $P = .9042$; Figure 1e, $n = 5$, unpaired t-test, $t_{(8)} = 2.124$; $P = .0664$). To further validate this result, we remeasured the retinal thickness using OCT (Figure S1a, at a similar retinal position as the histological section), which also did not so show any statistically significant difference either between the C57BL/6 and *Gnat2*^{cpfl3} RA mice at P17 and 6 months (Figure S1b, $n = 5$, unpaired t-test, $t_{(8)} = .7641$; P = .4667; Figure S1c, unpaired t-test, $n = 5$, $t_{(8)} = .6361$; $P = .5425$). Next, we counted the number of cells in the retinal ONL in histological sections at P17 and 6 months. Here, the *Gnat2*^{cpfl3} RA mice showed significantly fewer cells in the ONL compared to C57BL/6 RA mice at 6 months (Figure 1f, $^{**}P < .01$, $n = 10$, unpaired t-test, $t_{(18)} = 3.640$; $P = .0019$), but not at P17 (Figure 1c, n = 10, unpaired t-test, $t_{(18)} = .8293$; $P = .4178$). Taken together, these results demonstrate that *Gnat2*^{cpfl3} RA mice initially retain complete retinal structural integrity (up to P17) but develop slow retinal degeneration in the ONL in adulthood.

3.2 Abnormal interplay between transducin and PDE6 induces cone cell dysfunction

To monitor retinal function, the mice were examined using full-field ERG under light- and dark-adapted conditions at P17. Under dark-adapted conditions (Figure S2a), the amplitudes of neither the a-wave nor the b-wave showed any significant difference between C57BL/6 and

Gnat2^{cpfl3} RA mice (Figure S2b, $n = 5$, unpaired t-test, $t_{(8)} = .2013$; $P = .8455$; Figure S2c, $n = 5$, unpaired t-test, $t_{(8)} = .616$; $P = .555$), indicating normal rod-mediated responses in the latter. In contrast, after exposure to light for 15 min (Figure 2a, to saturate the rod cell response and record the cone cell response without rod interference), the photopic response was almost entirely absent in the *Gnat2*^{cpfl3} RA mice (Figure 2b, $^{**}P < .01$, $n = 5$, Mann–Whitney U test, $P = .0079$; Figure 2c, $^{**}P < .01$, $n = 5$, Mann–Whitney U test, $P = .0079$), suggesting profound cone cell dysfunction.

To investigate the mechanism of decreased cone cell sensitivity, western blot analysis was performed to compare the relative quantity of p-PDE6γ' protein in retinas of C57BL/6 versus *Gnat2*^{cpfl3} RA mice at P17 (Figure 2d). To maximize the cone-specific p-PDE6γ' expression and decrease the rod-specific p-PDE6γ activation, the mice were euthanized after 15 min exposure to light. This revealed a significant decrease in cone-specific p-PDE6γ' protein in the retinas of *Gnat2*^{cpfl3} mice at P17 (Figure 2e, $^{**}P < .01$, $n = 5$, unpaired t-test, $t_{(8)} = 4.2$; $P = .003$), whereas rod-specific p-PDE6γ was not statistically different between the two groups (Figure 2f, $n = 5$, unpaired t-test, $t_{(8)} = .7192$; $P = .4925$). These results suggest that an abnormal interaction between the mutant transducin and PDE6 induceed cone cell dysfunction.

3.3 *Gnat2*^{cpfl3} OIR mice exhibit a less hypoxic degree

Next, we used *Gnat2*^{cpfl3} mice to investigate the role of cone cell dysfunction in the OIR mouse model (Figure 3a). The retinal hypoxic area was measured in retinal whole-mounts at P14 by immunostaining with pimonidazole administered via intraperitoneal injection 30 min before sacrificing the animals (Figure 3b). This revealed that the hypoxic area in the C57BL/6 OIR mice was significantly greater than that in *Gnat2*^{cpfl3} OIR mice (Figure 3c, $^{*}P < .05$, $n = 5$,

unpaired t-test, $t_{(8)} = 2.64$; $P = .0297$). To establish the retinal layer in which hypoxia was located, cross-sections were prepared, which revealed distinct staining in the inner retina but not in the outer retina (Figure 3d). Immunofluorescence intensity was also significantly reduced in the cross sections of *Gnat2*^{cpfl3} OIR mice (Figure 3e, $^{*}P < .05$, $n = 10$, unpaired t-test, $t_{(8)} = 2.406$; $P = .0271$). To further verify these results, western blot was used to compare the relative quantity of HIF-1α expression in the retina from C57BL/6 and *Gnat2*^{cpfl3} OIR mouse eyes compared to age-matched RA controls at P14 (Figure 3f), revealing substantially lower amounts of HIF-1α in *Gnat2*^{cpfl3} OIR mice (Figure 3g, $^{*}P < .05$, $^{**}P < .01$, $n = 5$, two-way ANOVA with Bonferroni's post hoc analysis, genotype: $F_{(1, 16)} = 9.913$, $P = .062$, oxygen concentration: $F_{(1, 16)} = 22.79$, $P = .002$). Collectively, these findings suggest that the *Gnat2*^{cpfl3} OIR mice exhibit less hypoxia during the hypoxic phase of the OIR model.

3.4 Attenuated pathological neovascularization in *Gnat2*^{cpfl3} OIR mice

Next, the neovascular response was evaluated at P17. Fluorescent microscopy revealed extensive preretinal neovascular tufts, mainly located at the junction between the vascular and avascular regions (Figure 4a). Compared with the C57BL/6 OIR mice, the neovascular tufts were markedly attenuated in the *Gnat2*^{cpfl3} OIR mice (Figure 4b, $^{*}P < .05$, $n = 10$, unpaired t-test, $t_{(18)} = 2.824$; $P = .0112$). Moreover, the avascular area in the *Gnat2*^{cpfl3} OIR mice was decreased (Figure 4c, $^{*}P < .05$, $n = 10$, unpaired t-test, $t_{(18)} = 2.242$; $P = .0378$). H&E staining was performed to count the preretinal vascular cell nuclei breaking through the inner limiting membrane (Figure 4d). *Gnat2*^{cpfl3} OIR mice contained fewer cell nuclei in the vitreous compared to C57BL/6 OIR mice (Figure 4e, $^{*}P < .05$, $n = 20$, unpaired t-test, $t_{(38)} = 2.162$; $P = .037$). In addition, we observed subretinal hemorrhages in the C57BL/6 OIR mice, but not in the mutant mice.

Next, western blots were used to compare the relative quantity of VEGF expression in the retina from C57BL/6 and *Gnat2*^{cpfl3} OIR mouse eyes compared to age-matched RA controls at P14 (Figure 4f), the levels of VEGF protein were substantially lower in the *Gnat2*^{cpfl3} OIR mice (Figure 4g, $^{**}P < .01$, $n = 5$, two-way ANOVA with Bonferroni's post hoc analysis, genotype: $F_{(1, 16)} = 20.5$, $P = .003$, oxygen concentration: $F_{(1, 16)} = 17.28$, $P = .0007$). Altogether, these results suggest that *Gnat2*^{cpfl3} mice demonstrate attenuated neovascularization in the OIR model, due to reduced VEGF expression.

4 DISCUSSIONS

Previous clinical studies have reported that retinal neovascularization appears to infrequently coincide with retinal degeneration in patients (Hayakawa et al., 1993; Lahdenranta et al., 2001). Interestingly, to note that retinal neovascularization also seems to be mitigated in retinal degeneration mice within the OIR model (Lahdenranta et al., 2001; Scott et al., 2014; Zhang & Zhang, 2014). These observations support to the hypothesis that inner retinal hypoxia arises from elevated oxygen consumption by photoreceptor cells, suggesting that retinal oxygen demand is diminished in mice with retinal photoreceptor degeneration (Pennesi et al., 2008; Zhang & Zhang, 2014). Recent studies have suggested that the amacrine cells activity coordinates angiogenesis and blood-retinal barrier (BRB) formation, even in the absence of changes in cell number (Weiner et al., 2019). This finding suggests that neural activity may serve as a broad stimulator of angiogenesis. Therefore, it is pertinent to question whether the activity of other retinal neurons also contributes to angiogenesis.

Initially, we examined retinal histopathological and morphometric changes using histology and OCT. Our findings are consistent with those of previous reports, with the thickness measurements from histological sections being lower than those from OCT scans (Berger et al., 2014). Although the retinal thickness did not vary significantly between the two groups, it is noteworthy that the average cell numbers in the ONL were considerably reduced in *Gnat2*^{cpfl3} RA mice at 6 months. However, at P17, there was no loss of cells in the ONL, ruling out reduced cell numbers (and hence exhibited less hypoxia) as an explanation for our findings in the OIR model.

Our ERG measurements confirmed that *Gnat2*^{cpfl3} mice exhibited a normal scotopic response at P17 but almost completely lacked photopic responses at P17. Previous studies have suggested that reduced cone cell responses in *Gnat2*^{cpfl3} mice could be due to the abnormal

interaction between the mutant transducin and the effector molecule, PDE, in these mice (Chen et al., 2020). PDE6 is the effector enzyme in the visual system which is comprised of alpha/alpha homodimers and gamma inhibitory subunits in the cone cells (Yamazaki et al., 2010). Under light exposure, the PDE6γ inhibitory subunit is modified by phosphorylation to activate the phototransduction process (Janisch et al., 2009). Thus, to further investigate the mechanism of decreased cone cell activity in *Gnat2*^{cpfl3} mice, we analyzed the p-PDE6γ' protein using western blotting. Consistent with the ERG results, we found a significant reduction in cone-specific p-PDE6γ' expression in *Gnat2*^{cpfl3} mice at P17 (Figure 2). Our findings suggest that an abnormal interaction between mutant transducin and PDE6 causes cone cell dysfunction.

To evaluate the role of cone cell dysfunction in ischemic retinopathy, we used the OIR mouse model. A previous study showed that the hypoxic area was absent in *Pde6b*^{rd1} OIR mice (Scott et al., 2014). Therefore, we first examined the retinal hypoxic area using pimonidazole, which is specifically activated in hypoxic cells and forms a stable products (Aguilera & Brekken, 2014). We found both the retinal hypoxic area and pimonidazole immunostaining intensity were significantly reduced in *Gnat2*^{cpfl3} OIR mice at P14. Interestingly, based on high-magnification images of retinal cross-sections, we can speculate that most of the hypoxic cells are Müller cells (Figure 3), which is consistent with earlier reports suggesting that Müller cells are the primary source of VEGF in the inner retina (Stone et al., 1995). Moreover, retinal neovascularization was significantly attenuated in *Gnat2*^{cpfl3} OIR mice at P17, which is a primary characteristic of ROP (Sapieha et al., 2010; Selvam, Kumar, & Fruttiger, 2018). We also observed the subretinal hemorrhages in C57BL/6 mice, indicating more severe hypoxia in these mice.

The HIF-1α/VEGF pathway plays a critical role in the development of ROP and blocking HIF-1α/VEGF expression inhibits retinal neovascularization in the OIR mouse model (Park et

al., 2014; Selvam et al., 2018; Vadlapatla, Vadlapudi, & Mitra, 2013). Therefore, we measured HIF-1α and VEGF protein expression at P14, which is the period that reached a peak after return to room air in the OIR mouse model (Villacampa et al., 2017), and found decreased HIF-1α and VEGF protein expression in Gnat2^{cpfl3} OIR mice (Figure 3, Figure 4). These findings suggest that pathological neovascularization was attenuated in the Gnat2^{cpfl3} OIR mice due to reduced activity of the HIF-1α/VEGF axis.

Mounting evidence suggests that neural activity acts as an oxygen sensor that controls angiogenesis (Sapieha, 2012). During postnatal mouse cerebral cortex development, vascular density and branching were decreased when the sensory input is reduced (Lacoste et al., 2014). Direct evidence of retinal neurons influencing angiogenesis has been observed during retinal neuron differentiation, which coincides with retinal vasculature development (Selvam et al., 2018). A likely explanation for this phenomenon is that the increased oxygen consumption and metabolic requirements of the newly differentiated neurons lead to angiogenesis (Cringle, Yu, Su, & Yu, 2006). Among these, photoreceptor cells account for at least half of the metabolic activity in the retina, and the role of rod cells in the OIR model has been confirmed (Akula et al., 2010; Du et al., 2013). Therefore, there is reason to suspect that cone cell activity can influence blood vessel behavior in ischemic retinopathy. Our results show that cone cell activity has an impact on pathological angiogenesis despite cones representing only 3% of all mouse retinal photoreceptors (Carter-Dawson & LaVail, 1979). It is possible that Müller cells regulate angiogenesis by receiving signals from cones and other neurons (Li, Liu, Hoh, & Liu, 2019; Rosa et al., 2015), or that retinal neurons control non-neuronal cells (such as astrocytes) to produce VEGF (Selvam et al., 2018; Weiner et al., 2019). However, how exactly cone cell activity can influence the HIF-1α/VEGF pathway in ischemic retinopathy is not yet mechanistically understood.

5 CONCLUSIONS

In summary, we have described the role of cone cell function in the OIR mouse model. Mechanically, we found that attenuated neovascularization is associated with HIF-1α/VEGF axis in *Gnat2*^{cpfl3} OIR mice. These results suggest that retinal neural activity may precedes and potentially influences the onset of pathological neovascularization.

CONFLICT OF INTEREST

The authors declare that they have no known competing financial interests or personal relationships that could have appeared to influence the work reported in this paper.

AUTHOR CONTRIBUTIONS

All authors had full access to all the data in the study and take responsibility for the integrity of the data and the accuracy of the data analysis. *Conceptualization*, M.F. and J.H.K.; *Methodology*, M.F. and J.H.K.; *Investigation*, J.W. and D.H.J.; *Data Curation,* J.W. and D.H.J.; *Formal Analysis*, J.W. and M.F.; *Writing – Original Draft*, J.W.; *Writing – Review & Editing*, M.F. and J.H.K.; *Supervision*, M.F. and J.H.K.; *Project Administration*, J.H.K.; *Funding Acquisition*, J.H.K.

DATA AVAILABILITY STATEMENT

The data that support the findings of this study are available from the corresponding author upon reasonable request.

ACKNOWLEDGMENTS

This study was supported by Kun-hee Lee Child Cancer & Rare Disease Project, Republic of Korea (202200004004 to J.H.K.), Seoul National University Hospital Research Grant (18-2023-0010 to J.H.K.), the Ministry of Trade, Industry, and Energy, and the Ministry of Health and Welfare (HN21C0917 to J.H.K.), the National Research Foundation of Korea (NRF) Grants (2015M3A7B6027946 to J.H.K.), the Korea Research Institute of Bioscience and Biotechnology (KRIBB) Research Initiative Program (KGM5362111 to J.H.K), and the Development of Platform Technology for Innovative Medical Measurement funded by Korea Research Institute of Standards and Science (KRISS-GP2022-0006 to J.H.K.).

DECLARATION OF TRANSPARENCY

The authors, reviewers and editors affirm that in accordance to the policies set by the *Journal of Neuroscience Research*, this manuscript presents an accurate and transparent account of the study being reported and that all critical details describing the methods and results are present.

REFERENCE

Aguilera, K. Y., & Brekken, R. A. (2014). Hypoxia Studies with Pimonidazole in vivo. *Bio Protoc, 4*(19). doi:10.21769/bioprotoc.1254

Akula, J. D., Hansen, R. M., Tzekov, R., Favazza, T. L., Vyhovsky, T. C., Benador, I. Y., . . . Fulton, A. B. (2010). Visual cycle modulation in neurovascular retinopathy. *Exp Eye Res, 91*(2), 153-161. doi:10.1016/j.exer.2010.04.008

Berger, A., Cavallero, S., Dominguez, E., Barbe, P., Simonutti, M., Sahel, J. A., . . . Bemelmans, A. P. (2014). Spectral-domain optical coherence tomography of the rodent eye: highlighting layers of the outer retina using signal averaging and comparison with histology. *PLoS One, 9*(5), e96494. doi:10.1371/journal.pone.0096494

Carter-Dawson, L. D., & LaVail, M. M. (1979). Rods and cones in the mouse retina. I. Structural analysis using light and electron microscopy. *J Comp Neurol, 188*(2), 245-262. doi:10.1002/cne.901880204

Chang, B., Dacey, M. S., Hawes, N. L., Hitchcock, P. F., Milam, A. H., Atmaca-Sonmez, P., . . . Heckenlively, J. R. (2006). Cone photoreceptor function loss-3, a novel mouse model of achromatopsia due to a mutation in Gnat2. *Invest Ophthalmol Vis Sci, 47*(11), 5017-5021. doi:10.1167/iovs.05-1468

Chen, N. S., Ingram, N. T., Frederiksen, R., Sampath, A. P., Chen, J., & Fain, G. L. (2020). Diminished Cone Sensitivity in cpfl3 Mice Is Caused by Defective Transducin Signaling. *Invest Ophthalmol Vis Sci, 61*(4), 26. doi:10.1167/iovs.61.4.26

Connor, K. M., Krah, N. M., Dennison, R. J., Aderman, C. M., Chen, J., Guerin, K. I., . . . Smith, L. E. (2009). Quantification of oxygen-induced retinopathy in the mouse: a model of vessel loss, vessel regrowth and pathological angiogenesis. *Nat Protoc, 4*(11), 1565-1573. doi:10.1038/nprot.2009.187

Cringle, S. J., Yu, P. K., Su, E. N., & Yu, D. Y. (2006). Oxygen distribution and consumption in the developing rat retina. *Invest Ophthalmol Vis Sci, 47*(9), 4072-4076. doi:10.1167/iovs.05-1638

Du, J., Cleghorn, W., Contreras, L., Linton, J. D., Chan, G. C., Chertov, A. O., . . . Hurley, J. B. (2013). Cytosolic reducing power preserves glutamate in retina. *Proc Natl Acad Sci U S A, 110*(46), 18501-18506. doi:10.1073/pnas.1311193110

Hayakawa, M., Hotta, Y., Imai, Y., Fujiki, K., Nakamura, A., Yanashima, K., & Kanai, A. (1993). Clinical features of autosomal dominant retinitis pigmentosa with rhodopsin gene codon 17 mutation and retinal neovascularization in a Japanese patient. *Am J Ophthalmol, 115*(2), 168-173. doi:10.1016/s0002-9394(14)73920-0

Hellström, A., Smith, L. E., & Dammann, O. (2013). Retinopathy of prematurity. *Lancet, 382*(9902), 1445-1457. doi:10.1016/s0140-6736(13)60178-6

Janisch, K. M., Kasanuki, J. M., Naumann, M. C., Davis, R. J., Lin, C. S., Semple-Rowland, S., & Tsang, S. H. (2009). Light-dependent phosphorylation of the gamma subunit of cGMP-phophodiesterase (PDE6gamma) at residue threonine 22 in intact photoreceptor neurons. *Biochem Biophys Res Commun, 390*(4), 1149-1153. doi:10.1016/j.bbrc.2009.10.106

Kim, C. B., D'Amore, P. A., & Connor, K. M. (2016). Revisiting the mouse model of oxygen-induced retinopathy. *Eye Brain, 8*, 67-79. doi:10.2147/eb.S94447

Lacoste, B., Comin, C. H., Ben-Zvi, A., Kaeser, P. S., Xu, X., Costa Lda, F., & Gu, C. (2014). Sensory-related neural activity regulates the structure of vascular networks in the cerebral cortex. *Neuron, 83*(5), 1117-1130. doi:10.1016/j.neuron.2014.07.034

Lahdenranta, J., Pasqualini, R., Schlingemann, R. O., Hagedorn, M., Stallcup, W. B., Bucana, C. D., . . . Arap, W. (2001). An anti-angiogenic state in mice and humans with retinal photoreceptor cell degeneration. *Proc Natl Acad Sci U S A, 98*(18), 10368-10373. doi:10.1073/pnas.181329198

Li, X., Liu, J., Hoh, J., & Liu, J. (2019). Müller cells in pathological retinal angiogenesis. *Transl Res, 207*, 96-106. doi:10.1016/j.trsl.2018.12.006

Liu, C. H., Wang, Z., Sun, Y., & Chen, J. (2017). Animal models of ocular angiogenesis: from development to pathologies. *Faseb j, 31*(11), 4665-4681. doi:10.1096/fj.201700336R

Pang, J., Thomas, N., Tsuchiya, D., Parmely, T., Yan, D., Xie, T., & Wang, Y. (2021). Step-by-step preparation of mouse eye sections for routine histology, immunofluorescence, and RNA in situ hybridization multiplexing. *STAR Protoc, 2*(4), 100879. doi:10.1016/j.xpro.2021.100879

Park, S. W., Kim, J. H., Kim, K. E., Jeong, M. H., Park, H., Park, B., . . . Kim, J. H. (2014). Beta-lapachone inhibits pathological retinal neovascularization in oxygen-induced retinopathy via regulation of HIF-1α. *J Cell Mol Med, 18*(5), 875-884. doi:10.1111/jcmm.12235

Park, S. W., Kim, J. H., Park, W. J., & Kim, J. H. (2015). Limbal Approach-Subretinal Injection of Viral Vectors for Gene Therapy in Mice Retinal Pigment Epithelium. *J Vis Exp*(102), e53030. doi:10.3791/53030

Pennesi, M. E., Nishikawa, S., Matthes, M. T., Yasumura, D., & LaVail, M. M. (2008). The relationship of photoreceptor degeneration to retinal vascular development and loss in mutant rhodopsin transgenic and RCS rats. *Exp Eye Res, 87*(6), 561-570. doi:10.1016/j.exer.2008.09.004

Rosa, J. M., Bos, R., Sack, G. S., Fortuny, C., Agarwal, A., Bergles, D. E., . . . Feller, M. B. (2015). Neuron-glia signaling in developing retina mediated by neurotransmitter spillover. *Elife, 4*. doi:10.7554/eLife.09590

Sapieha, P. (2012). Eyeing central neurons in vascular growth and reparative angiogenesis. *Blood, 120*(11), 2182-2194. doi:10.1182/blood-2012-04-396846

Sapieha, P., Joyal, J. S., Rivera, J. C., Kermorvant-Duchemin, E., Sennlaub, F., Hardy, P., . . . Chemtob, S. (2010). Retinopathy of prematurity: understanding ischemic retinal vasculopathies at an

extreme of life. *J Clin Invest, 120*(9), 3022-3032. doi:10.1172/jci42142

Scott, A., Powner, M. B., & Fruttiger, M. (2014). Quantification of vascular tortuosity as an early outcome measure in oxygen induced retinopathy (OIR). *Exp Eye Res, 120*, 55-60. doi:10.1016/j.exer.2013.12.020

Selvam, S., Kumar, T., & Fruttiger, M. (2018). Retinal vasculature development in health and disease. *Prog Retin Eye Res, 63*, 1-19. doi:10.1016/j.preteyeres.2017.11.001

Smith, L. E., Wesolowski, E., McLellan, A., Kostyk, S. K., D'Amato, R., Sullivan, R., & D'Amore, P. A. (1994). Oxygen-induced retinopathy in the mouse. *Invest Ophthalmol Vis Sci, 35*(1), 101-111.

Stahl, A., Chen, J., Sapieha, P., Seaward, M. R., Krah, N. M., Dennison, R. J., . . . Smith, L. E. (2010). Postnatal weight gain modifies severity and functional outcome of oxygen-induced proliferative retinopathy. *Am J Pathol, 177*(6), 2715-2723. doi:10.2353/ajpath.2010.100526

Stone, J., Itin, A., Alon, T., Pe'er, J., Gnessin, H., Chan-Ling, T., & Keshet, E. (1995). Development of retinal vasculature is mediated by hypoxia-induced vascular endothelial growth factor (VEGF) expression by neuroglia. *J Neurosci, 15*(7 Pt 1), 4738-4747. doi:10.1523/jneurosci.15-07-04738.1995

Vadlapatla, R. K., Vadlapudi, A. D., & Mitra, A. K. (2013). Hypoxia-inducible factor-1 (HIF-1): a potential target for intervention in ocular neovascular diseases. *Curr Drug Targets, 14*(8), 919-935. doi:10.2174/13894501113149990015

Vähätupa, M., Järvinen, T. A. H., & Uusitalo-Järvinen, H. (2020). Exploration of Oxygen-Induced Retinopathy Model to Discover New Therapeutic Drug Targets in Retinopathies. *Front Pharmacol, 11*, 873. doi:10.3389/fphar.2020.00873

Villacampa, P., Menger, K. E., Abelleira, L., Ribeiro, J., Duran, Y., Smith, A. J., . . . Bainbridge, J. W. B. (2017). Accelerated oxygen-induced retinopathy is a reliable model of ischemia-induced retinal neovascularization. *PLoS One, 12*(6), e0179759. doi:10.1371/journal.pone.0179759

Weiner, G. A., Shah, S. H., Angelopoulos, C. M., Bartakova, A. B., Pulido, R. S., Murphy, A., . . . Goldberg, J. L. (2019). Cholinergic neural activity directs retinal layer-specific angiogenesis and blood retinal barrier formation. *Nat Commun, 10*(1), 2477. doi:10.1038/s41467-019-10219-8

Yamazaki, A., Bondarenko, V. A., Matsuura, I., Tatsumi, M., Kurono, S., Komori, N., . . . Usukura, J. (2010). Mechanism for the regulation of mammalian cGMP phosphodiesterase6. 1: identification of its inhibitory subunit complexes and their roles. *Mol Cell Biochem, 339*(1-2), 215-233. doi:10.1007/s11010-010-0387-8

Zhang, Q., & Zhang, Z. M. (2014). Oxygen-induced retinopathy in mice with retinal photoreceptor cell degeneration. *Life Sci, 102*(1), 28-35. doi:10.1016/j.lfs.2014.02.023

FIGURE LEGENDS

Figure 1: *Gnat2*^{cpfl3} mice have slow retinal degeneration properties

(a) Representative H&E staining images of C57BL/6 and *Gnat2*^{cpfl3} RA mice at P17. RA refers to the mice that have not undergone hyperoxia. Scale bar: 200 μm (top), 20 μm (bottom). (b) Quantification of retinal thickness between the inner limiting membrane to the retinal pigment epithelial layer at a location 200 μm away from the optic head in each group at P17 (n = 5, unpaired t-test, $t_{(8)}$ = .1243; P = .9042). (c) Quantification of the cell number of the ONL per 20 μm in each group at P17 (n =10, unpaired t-test, $t_{(18)}$ = .8293; P = .4178). (d) Representative H&E staining images of C57BL/6 and *Gnat2*^{cpfl3} mice RA at 6 months. Scale bar: 200 μm (top), 20 μm (bottom). (e) Quantification of retinal thickness between the inner limiting membrane to the retinal pigment epithelial layer at a location 200 μm away from the optic head in each group at 6 months (n = 5, unpaired t-test, $t_{(8)}$ = 2.124; P = .0664). (f) Quantification of the cell number of the ONL per 20 μm in each group at 6 months (**P < .01, n = 10, unpaired t-test, $t_{(18)}$ = 3.640; P = .0019). Data are presented as box and whisker plots with individual data points. The horizontal line inside the boxes denotes the median, the lower and upper lines of the boxes are the 25th and 75th percentiles of the dataset, respectively, and the whiskers mark the minimum and maximum values. RA, room air; H&E, hematoxylin and eosin; ONL, outer nuclear layer.

Figure 2: Abnormal interaction of Gnat2 and PDE6 induces cone cell dysfunction

(a) Representative photopic ERG waveform in C57BL/6 and *Gnat2*^{cpfl3} RA mice at P17. RA refers to the mice that have not undergone hyperoxia. Scale bars: 30 ms (x-axis) and 50 μV (y-axis). (b) Amplitudes of a-waves of photopic response of C57BL/6 and *Gnat2*^{cpfl3} RA mice at P17 (**P < .01, n = 5, Mann–Whitney U test, P = .0079). (c) Amplitudes of b-waves of

photopic response of C57BL/6 and *Gnat2*^{cpfl3} RA mice at P17 (**P < .01, n = 5, Mann–Whitney U test, P = .0079). (d) Western blot showing the protein expression levels of p-PDE6γ' (cone-specific) and p-PDE6γ (rod-specific) in C57BL/6 and *Gnat2*^{cpfl3} RA mice at P17. (e) The boxplot showed the densitometric analysis of the levels of p-PDE6γ' to β-actin (**P < .01, n = 5, unpaired t-test, $t_{(8)}$ = 4.2; P = .003). (f) Boxplot of densitometric analysis of levels of p-PDE6γ compared to β-actin (Figure 2f, n = 5, unpaired t-test, $t_{(8)}$ = .7192; P = .4925). Data are presented as box and whisker plots with individual data points. The horizontal line inside the boxes denotes the median, the lower and upper lines of the boxes are the 25th and 75th percentiles of the dataset, respectively, and the whiskers mark the minimum and maximum values. ERG, electroretinography; RA, room air; PDE, phosphodiesterase.

Figure 3: *Gnat2*^{cpfl3} mice demonstrates less hypoxic degree in OIR model

(a) Schematic experimental timeline of tissue preparation in the OIR. (b) Pimonidazole immunostaining was detected retinal hypoxic area (HP, red) and vessels were counterstained with Isolectin B4 (green) in OIR model of C57BL/6 and *Gnat2*^{cpfl3} mice at P14. Scale bars: 500 μm. (c) Quantification of retinal hypoxic area as percent of total areas of retinas from either the C57BL/6 and *Gnat2*^{cpfl3} OIR mice (*P < .05, n = 5, unpaired t-test, $t_{(8)}$ = 2.64; P = .0297). (d) Retinal cross-sections were prepared to detect retinal hypoxic area (HP, red) and nuclei were stained with DAPI (blue) in OIR model of C57BL/6 and *Gnat2*^{cpfl3} mice at P14. Scale bars: 200 μm (top), 20 μm (bottom). (e) Quantification of immunofluorescence intensity of hypoxia (*P < .05, n = 10, unpaired t-test, $t_{(8)}$ = 2.406; P = .0271). (f) Immunoblot analysis of HIF-1α protein expression in retina from OIR mouse eyes compared to age-matched room air controls at P14. (g) The boxplot showed the densitometric analysis of the levels of HIF-1α to β-actin (*P < .05, **P < .01, n = 5, two-way ANOVA with Bonferroni's post hoc analysis, genotype:

538 $F_{(1, 16)} = 9.913$, $P = .062$, oxygen concentration: $F_{(1, 16)} = 22.79$, $P = .002$). Data are presented
539 as box and whisker plots with individual data points. The horizontal line inside the boxes
540 denotes the median, the lower and upper lines of the boxes are the 25th and 75th percentiles of
541 the dataset, respectively, and the whiskers mark the minimum and maximum values. OIR,
542 oxygen-induced retinopathy; HP, hypoxyprobe; HIF-1α, hypoxia-inducible factor 1 alpha;
543 DAPI, 4′,6-diamidino-2-phenylindole.
544
545 **Figure 4: Pathological neovascularization attenuated in *Gnat2*^{cpfl3} OIR mice**
546 (a) Retinal whole-mount from C57BL/6 and *Gnat2*^{cpfl3} OIR retinas stained Isolectin B4 (green)
547 showing the neovascular area and avascular area at P17. White solid areas indicate avascular
548 areas and white dots indicate neovascularization. Scale bars: 500 μm. (b) Quantification of
549 retinal neovascular area as percent of total areas of retinas from either the C57BL/6 and
550 *Gnat2*^{cpfl3} OIR mice (*$P < .05$, $n = 10$, unpaired t-test, $t_{(18)} = 2.824$; $P = .0112$). (c)
551 Quantification of retinal neovascular area as percent of total areas of retinas from OIR model
552 of C57BL/6 and *Gnat2*^{cpfl3} mice (*$P < .05$, $n = 10$, unpaired t-test, $t_{(18)} = 2.242$; $P = .0378$). (d)
553 H&E-stained retinal cross-sections were prepared from C57BL/6 and *Gnat2*^{cpfl3} OIR mice at
554 P17. Red arrows indicate subretinal hemorrhage and black arrows indicate preretinal
555 neovascular cell nuclei. Scale bars: 200 μm (top), 20 μm (bottom). (e) Quantitative analysis of
556 neovascular cell nuclei from C57BL/6 and *Gnat2*^{cpfl3} OIR mice in each section (*$P < .05$, $n =$
557 20, unpaired t-test, $t_{(38)} = 2.162$; $P = .037$). (f) Immunoblot analysis of VEGF protein
558 expression in retina from OIR mouse eyes compared to age-matched room air controls at P14.
559 (g) The boxplot showed the densitometric analysis of the levels of VEGF to β-actin (**$P < .01$,
560 $n = 5$, two-way ANOVA with Bonferroni's post hoc analysis, genotype: $F_{(1, 16)} = 20.5$, $P = .003$,
561 oxygen concentration: $F_{(1, 16)} = 17.28$, $P = .0007$). Data are presented as box and whisker plots

562 with individual data points. The horizontal line inside the boxes denotes the median, the lower
563 and upper lines of the boxes are the 25th and 75th percentiles of the dataset, respectively, and
564 the whiskers mark the minimum and maximum values. OIR, oxygen-induced retinopathy;
565 H&E, hematoxylin and eosin; VEGF, vascular endothelial growth factor.
566

SUPPORTING INFORMATION

Supplementary Figure 1: OCT images exhibit normal retinal thickness

(a) Representative of OCT retinal images obtained from the C57BL/6 and *Gnat2*^{cpfl3} RA mice at P17 and 6 months. RA refers to the mice that have not undergone hyperoxia. (b) Quantification of retinal thickness between the inner limiting membrane to the retinal pigment epithelial layer at a location 200 μm away from the optic head in each group at P17 (n = 5, unpaired t-test, $t_{(8)}$ = .7641; P = .4667). (c) Quantification of retinal thickness between the inner limiting membrane to the retinal pigment epithelial layer at a location 200 μm away from the optic head in each group at 6 months (unpaired t-test, n = 5, $t_{(8)}$ = .6361; P = .5425). Data are presented as box and whisker plots with individual data points. The horizontal line inside the boxes denotes the median, the lower and upper lines of the boxes are the 25th and 75th percentiles of the dataset, respectively, and the whiskers mark the minimum and maximum values. OCT: optical coherence tomography; RA, room air.

Supplementary Figure 2: *Gnat2*^{cpfl3} mice have normal rod cell function

(a) Representative scotopic ERG waveform in C57BL/6 and *Gnat2*^{cpfl3} RA mice at P17. RA refers to the mice that have not undergone hyperoxia. Scale bars, 30 ms (x-axis) and 100 μV (y-axis). (b) Amplitudes of a-of scotopic response of C57BL/6 and *Gnat2*^{cpfl3} RA mice at P17 (n = 5, unpaired t-test, $t_{(8)}$ = .2013; P = .8455). (c) Amplitudes of b-waves of scotopic response of C57BL/6 and *Gnat2*^{cpfl3} RA mice at P17 (n = 5, unpaired t-test, $t_{(8)}$ = .616; P = .555). Data are presented as box and whisker plots with individual data points. The horizontal line inside the boxes denotes the median, the lower and upper lines of the boxes are the 25th and 75th percentiles of the dataset,

590 respectively, and the whiskers mark the minimum and maximum values. ERG,
591 electroretinography; RA, room air.
592

FIGURES

Figure 1

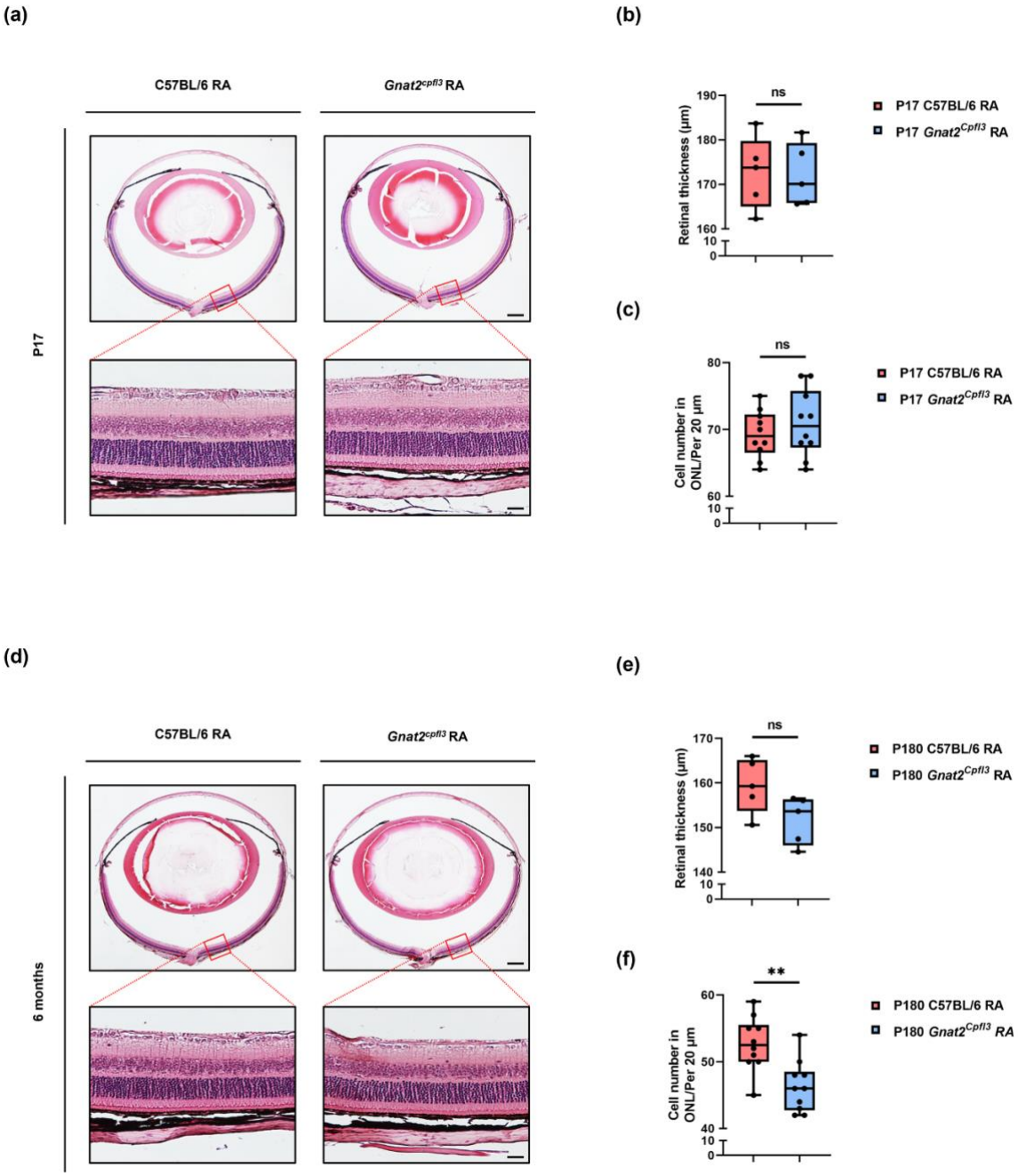

Figure 2

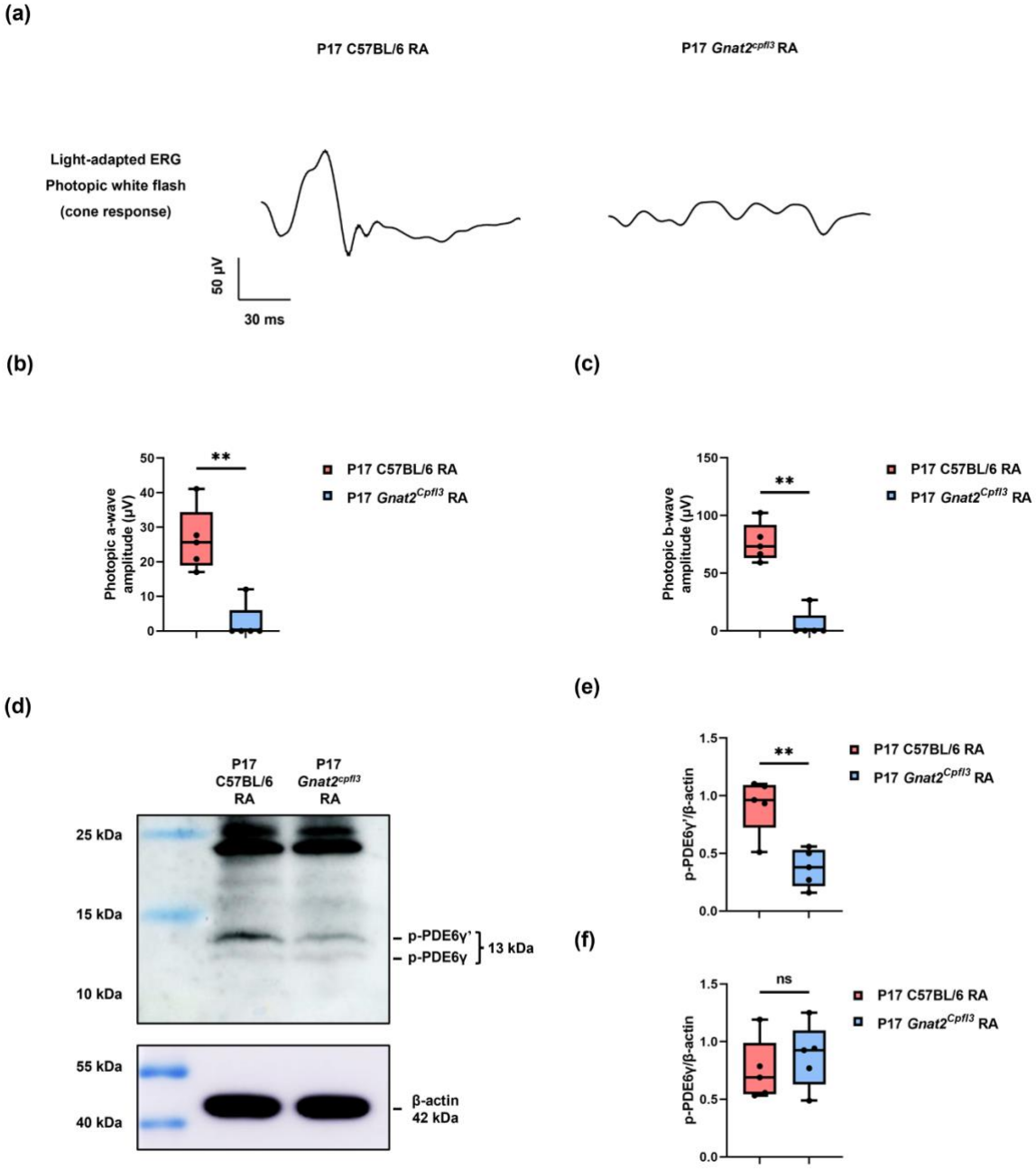
(a)
P17 C57BL/6 RA
P17 Gnat2cpfl3 RA
Light-adapted ERG
Photopic white flash
(cone response)
50 µV
30 ms
(b)
Photopic a-wave amplitude (µV)
**
P17 C57BL/6 RA
P17 Gnat2Cpfl3 RA
(c)
Photopic b-wave amplitude (µV)
**
P17 C57BL/6 RA
P17 Gnat2Cpfl3 RA
(d)
P17 C57BL/6 RA
P17 Gnat2cpfl3 RA
25 kDa
15 kDa
10 kDa
p-PDE6γ'
p-PDE6γ
13 kDa
55 kDa
40 kDa
β-actin
42 kDa
(e)
p-PDE6γ'/β-actin
**
P17 C57BL/6 RA
P17 Gnat2Cpfl3 RA
(f)
p-PDE6γ/β-actin
ns
P17 C57BL/6 RA
P17 Gnat2Cpfl3 RA

Figure 3

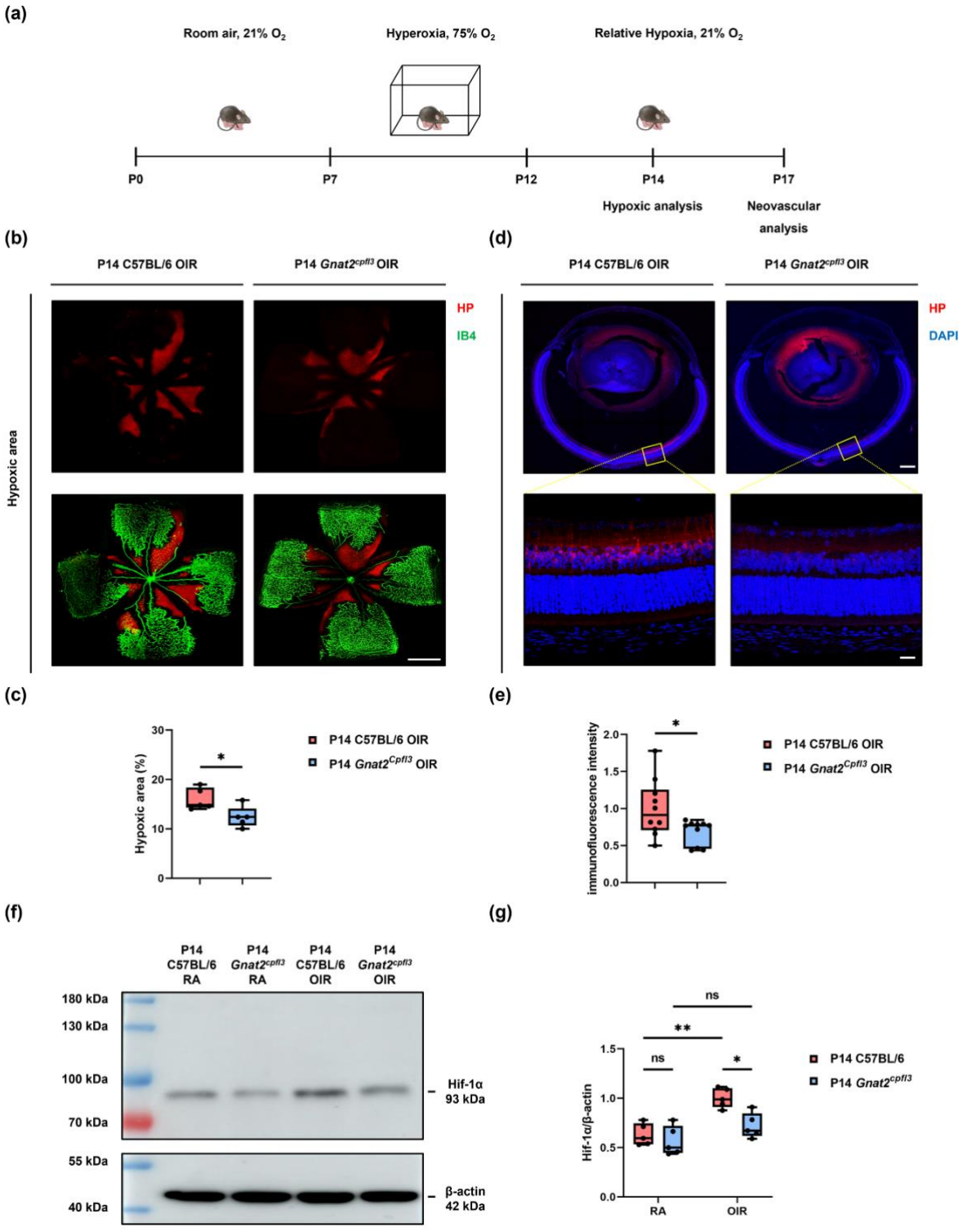
(a)
Room air, 21% O2
Hyperoxia, 75% O2
Relative Hypoxia, 21% O2
P0
P7
P12
P14
P17
Hypoxic analysis
Neovascular analysis
(b)
P14 C57BL/6 OIR
P14 Gnat2cpfl3 OIR
HP
IB4
Hypoxic area
(d)
P14 C57BL/6 OIR
P14 Gnat2cpfl3 OIR
HP
DAPI
(c)
Hypoxic area (%)
P14 C57BL/6 OIR
P14 Gnat2Cpfl3 OIR
(e)
immunofluorescence intensity
P14 C57BL/6 OIR
P14 Gnat2Cpfl3 OIR
(f)
P14 C57BL/6 RA
P14 Gnat2cpfl3 RA
P14 C57BL/6 OIR
P14 Gnat2cpfl3 OIR
180 kDa
130 kDa
100 kDa
70 kDa
55 kDa
40 kDa
Hif-1α 93 kDa
β-actin 42 kDa
(g)
Hif-1α/β-actin
ns
**
*
RA
OIR
P14 C57BL/6
P14 Gnat2cpfl3

603 **Figure 4**

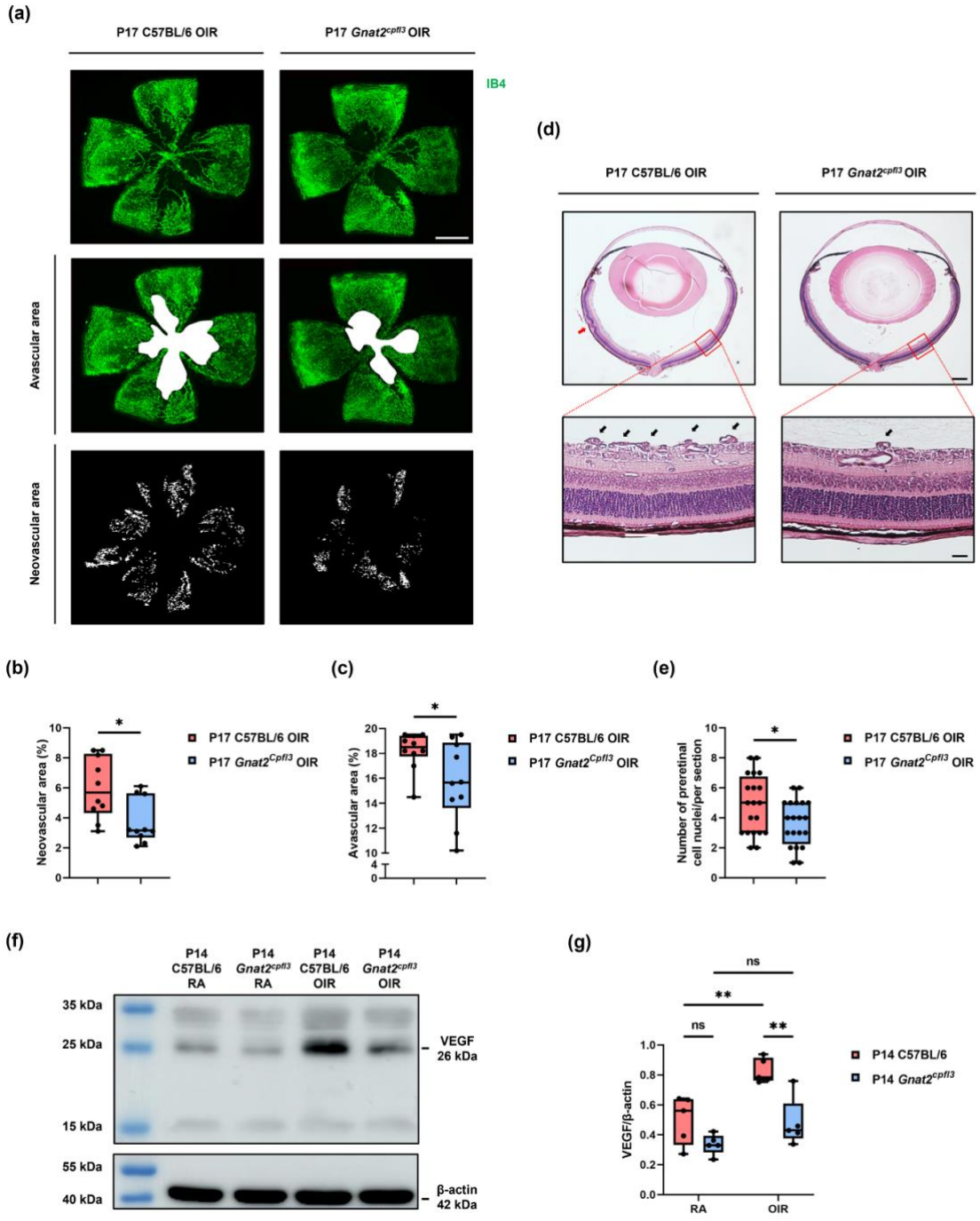

604

605

606 **Suppl. Figure 1**

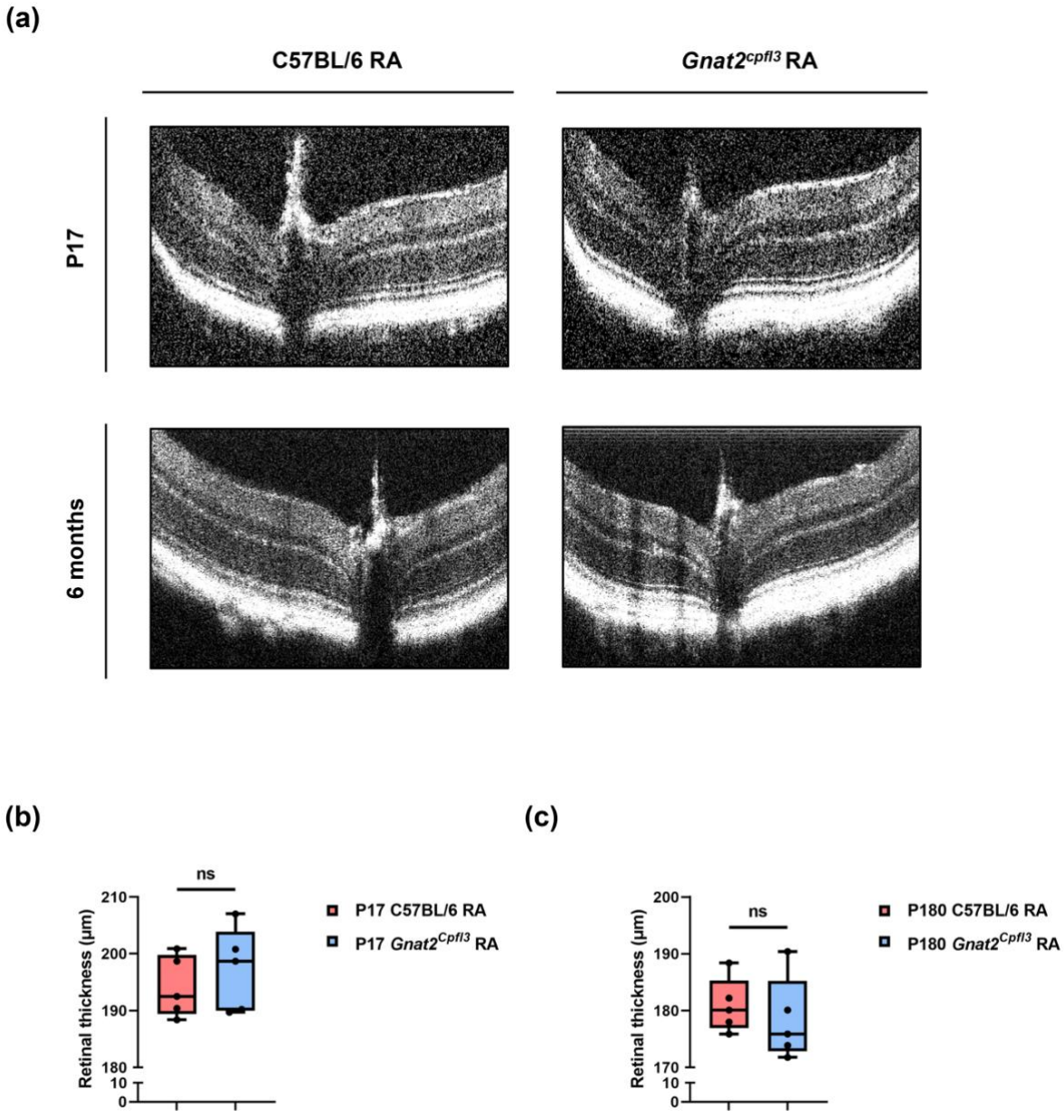

607

608

609 **Suppl. Figure 2**

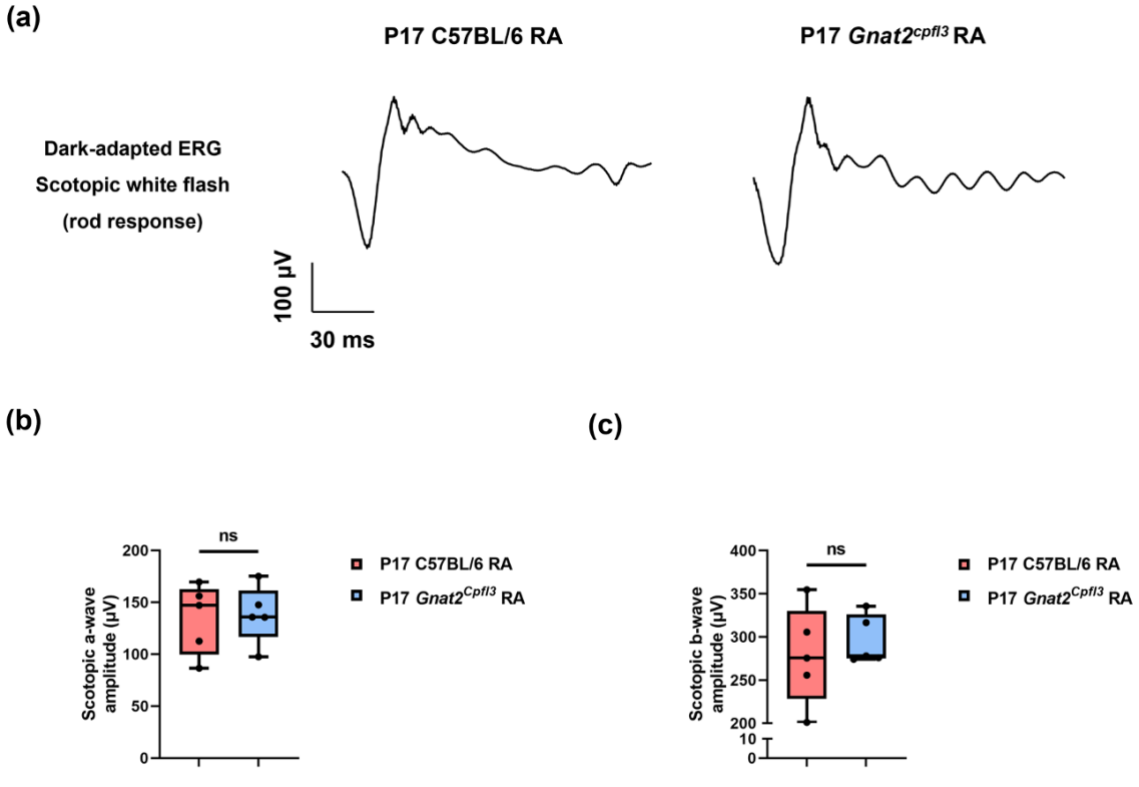

610

611

612

613 **Graphical Abstract**

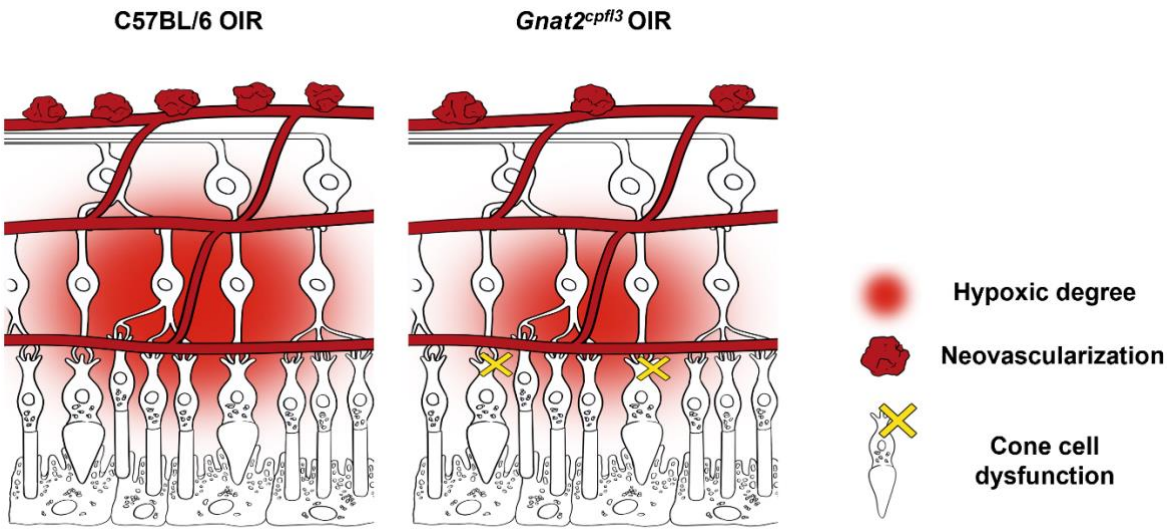

614